This is a repository copy of *Shock control of a low-sweep transonic laminar flow wing*.

Article:

Shock Control of a Low-Sweep Transonic Laminar Flow Wing

Maolin Zhu[1,3], Yonghong Li[2,3], Ning Qin[*3], Yong Huang[2], Feng Deng[1], Yibin Wang[1], Ning Zhao[1]

1 College of Aerospace Engineering, Nanjing University of Aeronautics and Astronautics, Nanjing, China
2 High-Speed Aerodynamics Institute, China Aerodynamics Research and Development Center, Mianyang. China
3 Department of Mechanical Engineering, The University of Sheffield, Sheffield, UK.

Abstract

This paper presents a combined experimental and computational study of a low-sweep transonic natural laminar flow (NLF) wing with shock control bumps (SCBs). A transonic NLF wing with a relatively low sweep angle of 20° was chosen for this study. To avoid the complexity of the flow introduced by perforated/slotted walls commonly used for transonic wind tunnel tests for reducing the wall interference, both experimental tests and computational simulations were conducted with solid wind tunnel wall conditions. This allows for like-to-like validation of the computational simulation. Optimization of the shock control bumps was first conducted to design the wind tunnel test model with bumps. Two critical parameters of the three-dimensional SCBs for shock control, i.e. bump crest position and bump height, were optimized in terms of total drag reduction at the given design point in the wind tunnel. We show that the strong shock wave on the low sweep NLF wing can be effective controlled by well-designed SCBs deployed along the wing span. The optimized SCBs result in 18.5% pressure drag reduction with 5% viscous drag penalty and the SCBs also bring some benefits at off-design conditions. The wind tunnel tests include pressure measurement, Particle Image Velocimetry (PIV), as well as Temperature Sensitive paint (TSP) to provide detailed insight into the shock control flow field and to validate the computational simulations. Comparisons include surface pressure profile, velocity distribution and transition location.

Nomenclature

α	=	angle of attack
c	=	chord length
C_D	=	drag coefficient
C_L	=	lift coefficient
C_p	=	pressure coefficient
C_{fx}	=	skin friction coefficient in the streamwise direction
d	=	width of the wind tunnel
h	=	height of bump crest
I	=	fluorescence intensity

---

[*] Professor of Aerodynamics, AIAA Associate Fellow, Corresponding Author.

k	=	turbulence kinetic energy
L	=	length of the wind tunnel test section
M	=	Mach number
Re_c	=	Reynolds number based on chord length
Re_θ	=	Reynolds number based on momentum thickness
x,y,z	=	Cartesian coordinates in streamwise, vertical and spanwise directions, respectively.

x_{crest}	=	streamwise position of bump crest
x_{tr}	=	transition onset location
$x_{tr,avg}$	=	average transition onset location
ω	=	turbulence dissipation ratio
γ	=	intermittency factor

NLF	=	natural laminar flow
SCB	=	shock control bump
CNC	=	Computer Numerical Control

1 Introduction

In Europe's vision for future air transport, Fight Path 2050 [1] published by Advisory Council for Aeronautics Research in Europe (ACARE) in 2011 sets a challenging target for a 75% reduction of CO_2 emissions from 2000 reference, which necessitates significant further reduction of aerodynamic drag for future aircraft. For modern transport aircraft, as much as 50 percent of the total drag comes from skin friction [2]. Extending the portion of laminar flow on the wing surface is one of the approaches to reduce skin friction drag which offers a large potential economic savings and improvements in environmental protection. Hybrid laminar flow control (HLFC) and natural laminar flow (NLF) are two main approaches to laminar flow. However, the efficiency of drag reduction of HLFC is severely limited by the price of pumping system. Atkin [3] found that HLFC decreased the total drag by 1.6 per cent, while it dropped to 1 per cent when taking pumping system into consideration. The research of NLF technology dates back to the 1940s when NACA 6-series airfoils [4] were firstly developed and the feasibility of it has been revealed by some early works [5]-[8]. At present, NLF technology is still an active research topic. In 2006, Cella et al. [9][10] designed a transonic NLF wing, UW-5006, referring to a medium-sized business-jet-class aircraft and experiments were conducted in wind tunnel. Recently, Hue et al. [11][12] and Xu et al. [13] conducted some experimental and computational research of transonic NLF wing. The up to date "Breakthrough Laminar Aircraft Demonstrator in Europe" (BLADE) project tried to move from the aerodynamic

concepts of natural laminar flow through to its industrialization and operational demonstration at full scale [14][15]. The flight test vehicle was based on an A340 with some structural changes to meet the need of natural laminar flow including the notably reduced sweep angle.

A major advance in modern transonic wing design is the introduction of wing sweep, typically over 30° to alleviate the shock effects and the resulting drag rise at transonic cruise [16]. On the other hand, sweeping the wing also promotes leading edge attachment line transition [17] and cross-flow (C-F) instability of the boundary layer [18], which in turn triggers a turbulent boundary layer downstream on the wing, implying a higher skin friction drag as compared to laminar flow boundary layers. The understanding of the effects of sweep and pressure gradient on transition [19] indicates that Tollmien-Schlichting (T-S) instability dominates transition for wings with sweep angles up to 25°. For sweeps over 30°, cross-flow instability mode prevails. The experience of the ELFIN flying tests shows that 20° is a limit for the cross-flow stability of the boundary layer [20]. Reed and Saric gave a more thorough description of these transition mechanisms in [21]. Recent practical applications of natural laminar flow can be found on the nacelles on Boeing 787 [22], the winglet on the 737max [22] and the wing on the supersonic Honda business jet [23], with zero or very small sweep angles. Qin [16] proposed to break the conventional rule of large sweep for transonic wing design by investigating the possibility of reducing wing sweep to 20° or less through careful balance of the drag-rise Mach number and skin friction drag, also considering the potential of the reduction of the wing structural weight through reduced sweep. In this concept, shock control is a crucial factor as both NLF airfoil pressure distribution, requiring favorable streamwise pressure gradient, and lower wing sweep from current dominant higher sweep design result in stronger shock waves on the wing upper surface at transonic cruise. The main objective of the present research is to investigate the capability of the shock control bumps (SCBs) in tackling the shock effects for low sweep NLF wing with a combined experimental and computational investigation.

Shock control research for transonic wings date back to the early 1960s when Pearcey [24] applied vane vortex generators on a transonic wing. In 1992, Ashill et al. [25] first proposed 2D shock control bumps to reduce wave drag on laminar flow airfoils. After that, the European research project EUROSHOCK [26] conducted a thorough study of different shock control methods, including suction, ventilation and shock control bumps [27][28], and among them, shock control bumps were found to be the most effective shock control device [29].

The early research affirms shock control bump's ability in shock wave alleviation. These studies stimulated recent research concentrated on the detailed flow physics of SCBs aiming to integrate them to future aircraft design. In 2000, Birkemeyer et al. [30] investigated the shock control device of two-dimensional contour bumps experimentally and numerically on a transonic swept wing. They found the influence of sweep on the bump effectiveness was rather small and the drag reduction is slightly lower for the swept wing than the 2D airfoil, i.e. zero sweep, case. Qin et al. [31]-[33] proposed and optimized three-dimensional contour bumps for NLF transonic airfoils and wings. They introduced the three-dimensional contour SCBs to an un-swept natural laminar flow wing. Their studies show that optimized three-dimensional bumps could effectively reduce the wave drag in a wider operational range as compared with the 2D bumps. Their further research [16] showed that three-dimensional shock control bumps could enable robust control of shock strength for natural laminar flow wings at low sweep angles. McIntosh and Qin found [34] that the effectiveness of shock control bumps is largely insensitive to the location of transition onset. Some fundamental understanding of the flow physics for shock control bumps can be found in Barbinsky et al. [35]-[37]

for a wedge shock control bump mounted on the floor of a supersonic wind tunnels. As Bruce and Colliss [38] pointed out in their review, these experiments have the advantage of being inexpensive and repeatable; however, the baseline flow does not represent the pressure gradient around airfoils/wings.

While most detailed experimental studies of SCBs in the literature so far were limited to those directly mounted on the wind tunnel wall, König et al. [29] conducted experimental and numerical studies to evaluate the drag reduction of an array of discrete three-dimensional shock control bumps mounted on an un-swept supercritical wing. Approximately 10% drag reduction was achieved in the drag-rise region in their experiment. They suggested that the wall interferences led to a shift of the shock location and the computationally designed bumps were off-design for the wind tunnel condition.

In this study, a transonic NLF wing with a moderate 20° sweep was used as the test model in order to avoid the effects of cross-flow and attachment line transition. The present computational bump design and simulations were conducted in the solid-wall wind tunnel condition so that the conditions for the two approaches are closely matched. In the following sections, we will lay out how computational design has been used for the construction of the wind tunnel model and how the two were matched for this study of the shock control for a low sweep NLF wing at transonic condition. The comparison of the wind tunnel test data with the computational simulation is presented for surface pressure distribution from pressure taps, velocity field contours from particle image velocimetry and transition location from temperature sensitive paint. After the comparison of the experimental data with the computational simulation, some conclusions are drawn on the effectiveness of the 3D shock control bump array on reducing shock strength and the resulting drag reduction for the low sweep transonic NLF wing.

2 Experimental Arrangements

2.1 Wind tunnel set-up and test models

The experiments were conducted in a wind tunnel with a working Mach number ranging from 0.3 to 2.5, a total pressure at 95-235 kPa and a total temperature at 280-300 K in the China Aerodynamics Research and Development Center. The dimension of the cross-section and length of the wind tunnel test section are 0.6m×0.6m, and 1.775m, respectively. The wind tunnel was usually equipped with perforated upper and lower walls for testing at transonic conditions to reduce the strong wall interference. Although this makes the test data more relevant to free flight conditions with far field boundary conditions, it also makes it very difficult for mutual validation between the experimental data and computational simulations due to the difficulty in modelling the flow details of the perforated wind tunnel wall with many inclined holes along with the plenum chambers. In order to set up a better correspondence between the experimental tests and the computational simulations for validation, solid walls were employed for the wind tunnel walls, which allows a more accurate setup of the boundary conditions in the computational model.

Since the wind tunnel had not been set to conduct transonic experiments with solid-wall conditions, the quality of the flow-field in the test section was first recalibrated beforehand. In order to maintain uniformity of the flow speed in the core flow region along the streamwise direction, an expansion angle of 0.2° for the upper and lower walls was implemented, as shown in Figure 1 for Mach number between 0.71 and 0.79. Different symbolled lines correspond to different Mach number flow conditions. The symbols with lines show the slight variation of the Mach number along the streamwise direction in the wind tunnel test section from entrance to exit, where L is the test section length.
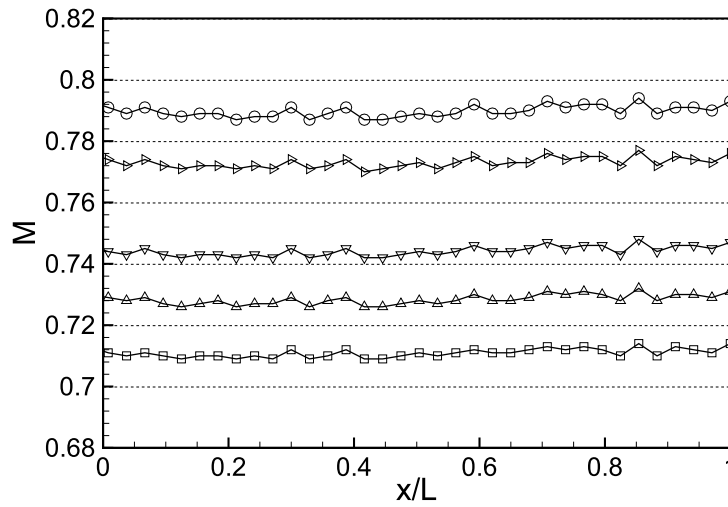
Fig. 1   Mach number distribution in the wind tunnel core flow region with 0.2° expansion angle

Two experimental wing models were made from high strength Grade 250 maraging steel using high precision Computer Numerical Control (CNC) machine with a tolerance of 1 Micron in x and y directions and 10 Microns in z direction. The Cartesian coordinates x, y and z correspond to the streamwise, vertical and spanwise directions, respectively, as shown in Figure 3. The models were strong enough to avoid deformation in the wind tunnel tests under aerodynamic loading and sufficiently accurate to match the computer design models with and without the shock control bumps. The models were checked with a three-coordinate detector to satisfactory accuracy. The baseline model is a 20° sweep laminar flow wing (B-LFW) and the shock-control model (SC-LFW) is the same wing with 7 shock-control-bumps equally distributed in the central 1/3 of the wing along the span which represents the white area in Figure 2. The models were fixed on the steel windows of the wind tunnel side walls. The angles of attack of the models can be adjusted by rotating the steel windows.

There are 44 pressure taps of 0.8 mm in diameter in the central section of the baseline wing with 15 on the pressure side and 29 on the suction side. The taps extend from the leading edge to 0.9c on the wing. On the SC-LFW, some taps were added near the bump considering a more complicated flow there due to the shock boundary-layer interaction. The pressure pipes in the model cavity were led outside of the wind tunnel and then connected with the electronic scanning valve.
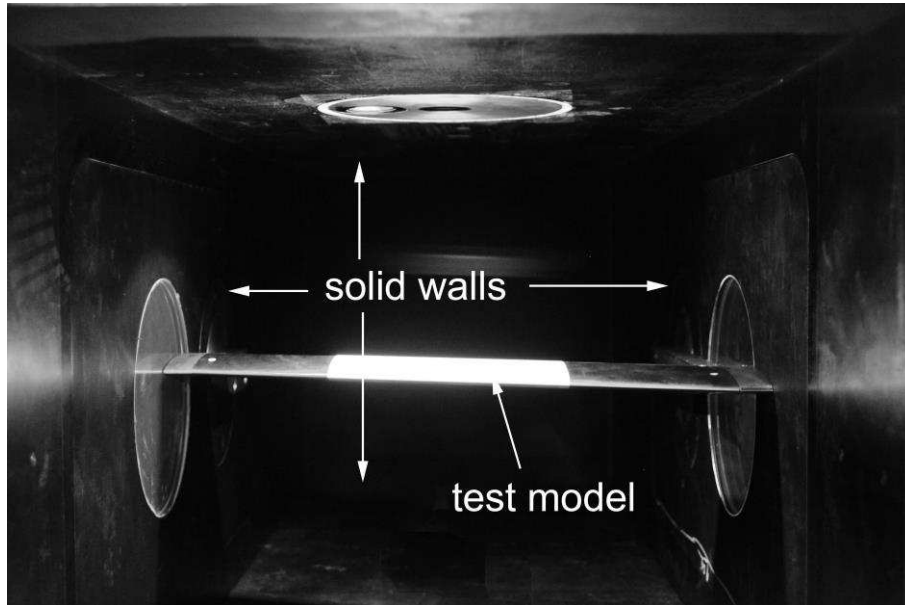
Fig. 2   Test model in the wind tunnel

2.2 Experimental measurements

The experimental measurement consists of five parts. The surface pressure was firstly measured by the pressure taps installed on the central section of the baseline wing and the SCB-wing, respectively. The particle image velocimetry (PIV) [39] technique was then used to give the velocity field information over the suction surface at the center section. Afterwards, transition locations were measured on the suction surface by the temperature sensitive paint (TSP) technique [12][40]. Only the middle one third of the wing was painted by TSP. Figure 2 shows the painted part of the wing in white on the wind tunnel model.

The wind tunnel was operated at an inlet total pressure of 104 kPa. The Mach number and angle of attack are 0.77 and 0° respectively for the design condition and Reynolds number, Re_c, based on the chord length equals to 2.6×10^6. Tests at different Mach numbers and angles of attack were conducted to investigate the flow characteristics and performance of SCBs at the off-design conditions. Mach numbers in the experiment were 0.75 and 0.77 and the angles of attack were changed within a small range (-0.5° to 0.5°). Higher Mach number results in shock reflection from the top wind tunnel wall and larger incidences lead to the choking problem.

3 CFD Set-up and Shock Control Bump Design

3.1 Numerical Methods

The computational study was performed by solving the Reynolds Average Navier-Stokes (RANS) equations using multi-block structured meshes to match the wing geometry and the wind tunnel geometry around it. At the inlet plane of the wind tunnel, stagnation pressure and temperature were prescribed and at the outlet, back pressure boundary condition was imposed for subsonic outflow condition. On the four walls of the wind tunnel and the model surface, no-slip boundary condition was set. A local time stepping method was employed for faster convergence. The governing equations were solved with second-order discretization. The SST γ-Re_θ transition model developed by Menter et

al. [41][42] is a four-equation turbulence closure consisting of the SST model coupled with two transport equations for the intermittency factor and the transition onset momentum thickness Reynolds number. Research of Lin et al. [43] shows that this model is capable of transition prediction in flows where T-S instability transition dominates and they applied it to transition prediction on a natural laminar flow nacelle. This turbulence model was used in this paper for the transitional flow cases. In order to investigate the effect of laminar boundary layer on the flow, the k-ω turbulence model [44] was also adopted for comparison in Sec. 4.1.

3.2 Computational domain of the test model

The NLF swept wing used here has a 20° sweep angle and a chord length of 0.2m. The maximum thickness of the wing is 11%c. The wing was mounted horizontally in the test section, as shown in Figures 3. Figure 4 gives the top view of the wind tunnel. The distances between wing leading edge and the upper and lower walls are both 0.3m. The distance between the wing leading edge on the side wall and the inlet is 0.7875 m. The shape of NLF airfoil aligned with the streamwise direction is shown in Figure 5. On the suction surface of the wing with SCBs, there are 7 identical shock control bumps installed along the spanwise direction, z-direction, with equal distance between 0.2m and 0.4m. The optimization of the bump shape is detailed below.
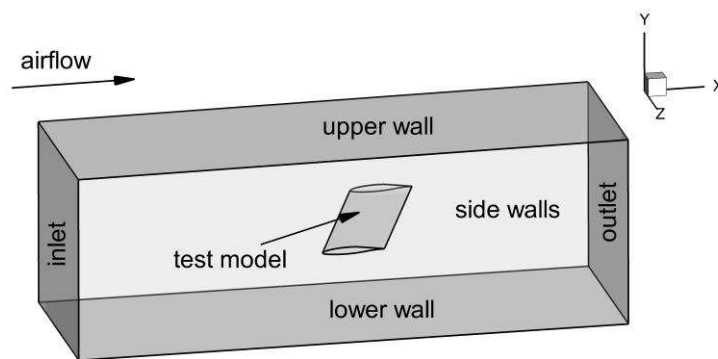

Fig. 3   Computational domain with the swept wing in the wind tunnel
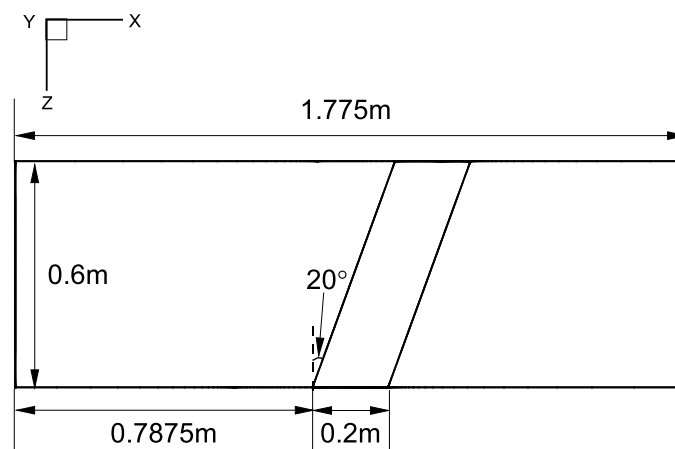

Fig. 4   Top View of the wind tunnel
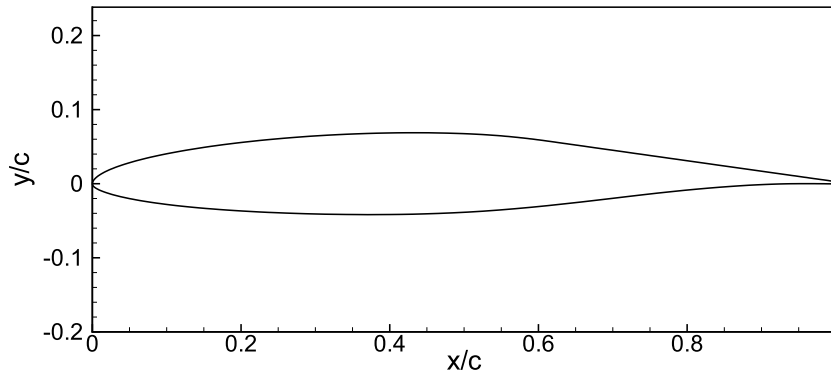
Fig. 5 Streamwise airfoil profile for the B-LFW wing model

Multi-block meshes were generated by the mesh generation software, Pointwise for both models. In order to obtain an orthogonal mesh near the wing surface, a C-type topology was adopted here, as shown in Figure 6. The meshes are clustered in the wall normal direction near the surface and in the vicinity of the leading and trailing edges and the shock wave area on the wing upper surface in the streamwise direction.

Grid sensitivity analysis was firstly carried out using grids of three different resolutions, namely a coarse mesh, a medium mesh and a fine mesh with cell numbers of approximately 6.4 million, 23.2 million and 45.8 million, respectively. The mesh refinement ratios between the coarse and medium grids in x, y and z directions are about 1.5. Figures 7 and 8 give the results of grid sensitivity analysis, showing the distributions of pressure coefficient and streamwise skin friction coefficient in the central section. The computed surface pressure does not show a strong sensitivity to grid resolution. However, some oscillations could be seen around the shock wave in the streamwise skin friction distributions in the coarse grid. The discrepancy between medium grid and fine grid is negligible. Based on the results of the grid sensitivity study, the medium grid was adopted. The overall grid size was 23.2 million. A total of 449×380 surface cells were placed on the wing surface in the streamwise and spanwise direction. There are 20 nodes in the spanwise direction for each shock control bump. Wall spacing on the wing and the wind tunnel walls was set to 1.5×10^{-6} to ensure $y^+\leq1$ on the no-slip walls to resolve the boundary layer.

a)   Computational grid   b)   Computational grid near the leading edge
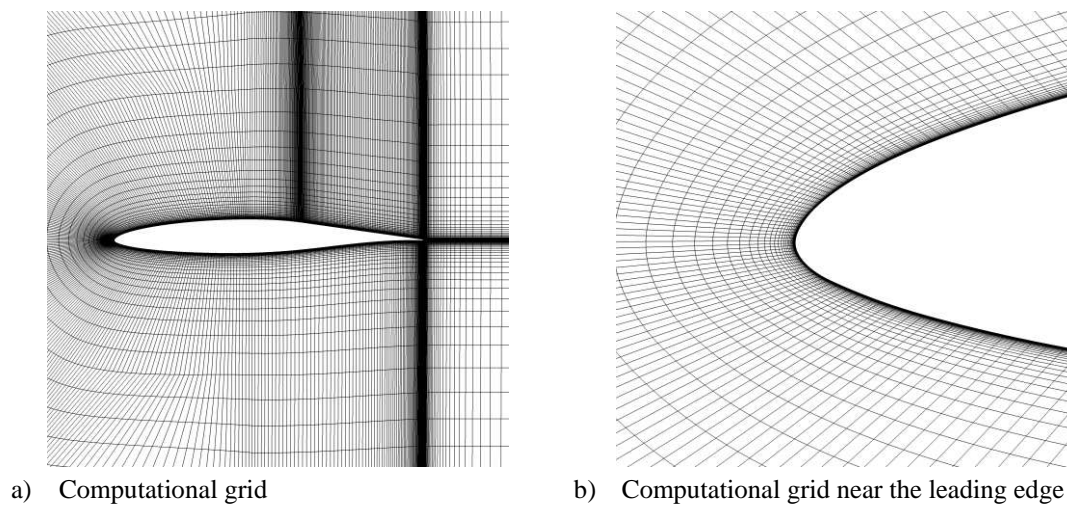
Fig. 6   C-type grid near the model in the central section
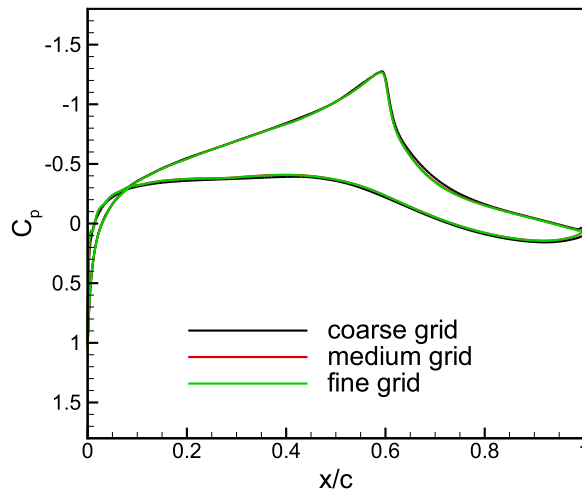
Fig. 7 Pressure coefficient in the central section, full turbulence boundary layer simulation
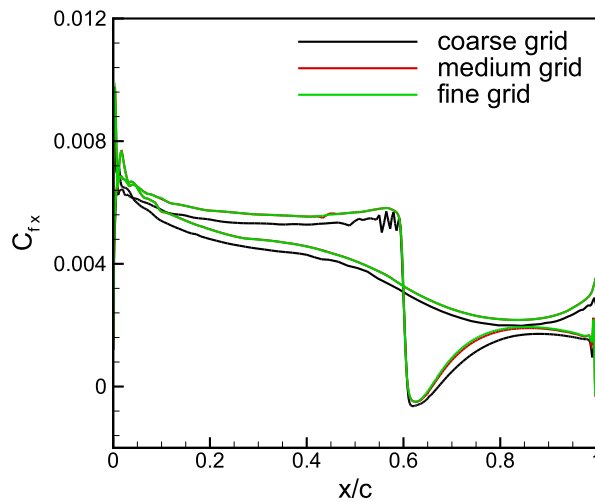
Fig. 8 Streamwise skin friction coefficient in the central section, full turbulence boundary layer simulation

3.3 Design of the three-dimensional shock control bump

In this research, the shock control bumps are aligned with the streamwise direction. Figure 9 shows the parameters for a three-dimensional contour shock control bump. The shape of the x-y plane at the middle section of the bump is generated by a cubic spline. Figure 10 gives the shape of the central section cut of the baseline wing and shock control wing. The same is used to model the variation in the y-z plane (cross-flow plane) shape across various chordwise locations of the bump, which then defines the full geometrical shape of the three-dimensional contour bump. The parameterized bumps are added to the swept wing upper surface for the wing with bumps. The bumps are not strictly symmetric in span direction because of the 20º sweep of the baseline wing. The bump surface gradient at base of the bump as well as the bump crest was set to be zero in order to maintain the continuity of the gradient at its intersection with the wing surface. The computational grid around the SC-LFW geometry is updated from B-LFW through an algebraic grid deformation technique that propagates the geometry change through the volume grid smoothly with the grid on wind tunnel walls

fixed.
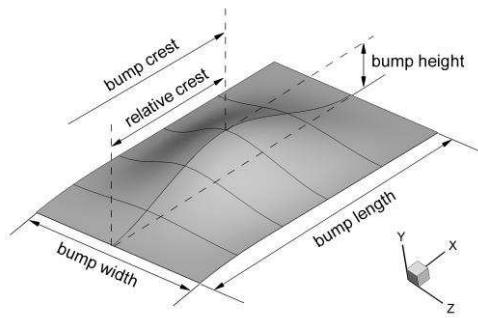
Fig. 9 SCB's geometry and parameterization
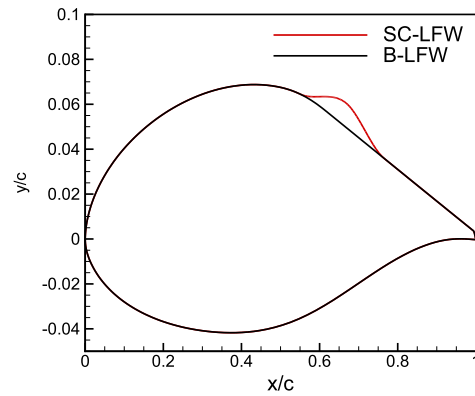
Fig. 10 The central section cut of B-LFW and SC-LFW

In order to achieve effective control of the shock wave in this experiment, optimization of bumps was conducted for the design condition in the wind tunnel. The operating conditions for this optimization is M=0.77, α=0°, and Re_c=2.6×10^6. Seven shock control bumps are installed equally spaced between z/d=0.33(Section 1) and z/d=0.67(Section 4). The middle bump's crest locates in the central section of the wind tunnel between Section 3 and 4. The location of these sections are shown in Figure 11. The distance between Sections 3 (z/d=0.476) and 4 (z/d=0.524) is the same as the width of the optimized shock control bump prescribed in the following paragraph. The wing model with shock control bumps is shown in Figure 12.
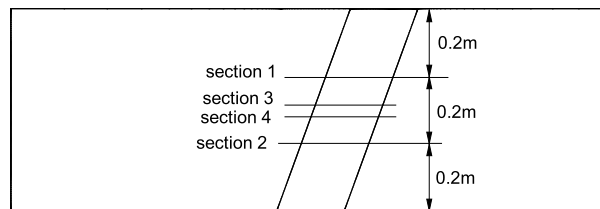

Fig. 11 Top view of the wing
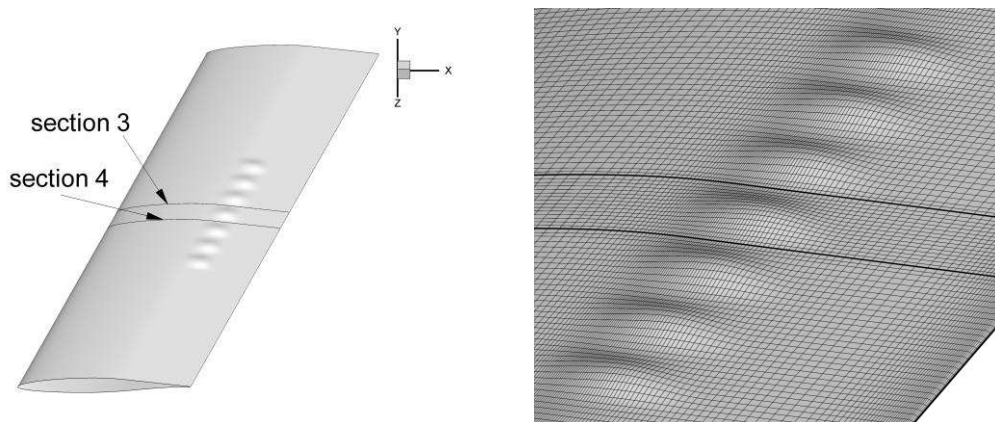
Fig. 12 Laminar flow wing with shock control bumps (Left) and the magnified surface around the middle bump (Right)

On the basis of our understanding of shock control bumps from previous work [16][31][32], the position of the bump crest in relation to the original shock wave and the height of the bump were found to be the two most sensitive parameters in the 3D contour bump design. In this research, these two key parameters were optimized to maximize the lift-to-drag ratio of the wing while the other less sensitive parameters were fixed based on the previous work. Specifically, we fixed the bump length at 0.215c, the relative crest position at 55% (of the bump length) and the width at 0.144c (to accommodate 7 bumps in the middle 1/3 span of the wing). The seven bumps are distributed consecutively along the span between z = 0.2m and 0.4m. During the optimization, the bump crest position, x_{crest}, varies between 65.8%c to 67.8%c as it was shown that the optimized bump crest location should be a little downstream to the original shock wave [32]. The bump height, h, varies between 0.85%c to 1.6%c. Considering the time-consuming RANS computations, the Radial Basis Function (RBF) approximation in the commercial multi-disciplinary optimization software, iSIGHT was adopted to approximate the surface for lift-to-drag ratio versus bump height and bump crest position. 12 design points were firstly evaluated to initialize the RBF approximation. Figure 13 gives the approximation surface and the optimization gave the best-performance bump height at 1.1%c and bump crest position at 66.8%c. The approximated lift-to-drag ratio, 23.20 shows a good agreement with the actual value obtained from the RANS solution, 23.32. Table 1 summarizes the values of these optimized parameters.
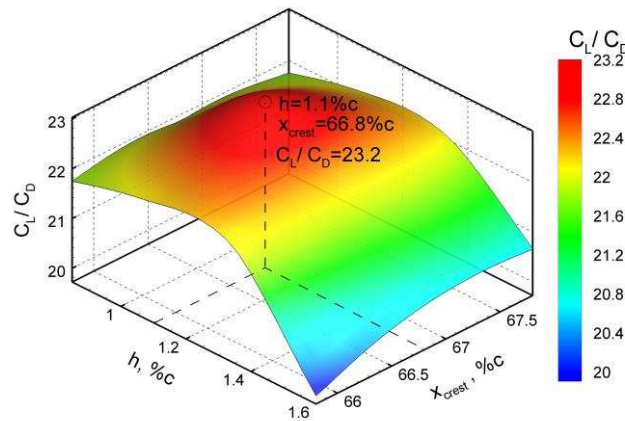

Fig. 13 Response surface of Lift-to-drag ratio for different bumps designs

Table 1 Parameters of the optimized bump, M=0.77, α=0°, Re_c =2.6×10⁶

Parameters	Length (%c)	Crest (%c)	Relative crest (%)	Width (%c)	Height (%c)
Optimized bump	21.5	66.8	55	14.4	1.1

The C_L/C_D ratio has increased from 18.69 for the B-LFW to 23.32 for the optimized SC-LFW. This optimized SC-LFW model was manufactured for the wind tunnel tests along with the B-LFW as presented in above sections.

4 Results and Discussions

4.1 Shock control effect on surface pressure

To validate the effects of shock control bumps on drag reduction, pressure distribution in the central section is firstly compared with the experimental data. Figure 14 gives the surface pressure

distributions in the central section of B-LFW from the experiments and the computations using the SST γ-Re$_\theta$ transition model and k-ω full turbulence model. In Figure 14, favorable pressure gradient is observed before a normal shock wave near 0.6c typical for a natural laminar flow wing. Compared with the results using the k-ω full turbulence model, employing the transition model with predicted transition on the wing smeared the peak pressure a little and gave a better agreement with the experiment. The small pressure plateau is due to the laminar separation bubble around the root of the shock wave which will be revealed in the later section on laminar-turbulent transition process. Therefore, the following computations in this research were all conducted using γ-Re$_\theta$ transition model with predicted transition rather than enforcing transition from the leading edge. As the 3D optimal contour bumps were applied, the pressure peak decreased and a good agreement was also achieved between the computational and experimental results of the shock-control wing, as shown in Figure 15. Figures 16 (a)-(f) compare the computational and experimental results at some off-design conditions. Both of them show that the favorable pressure gradient at these conditions is maintained and the position of shock wave is not sensitive to the small variations of Mach number and angle of attack. The decreased pressure peak also shows the effective shock control at these off-design conditions.
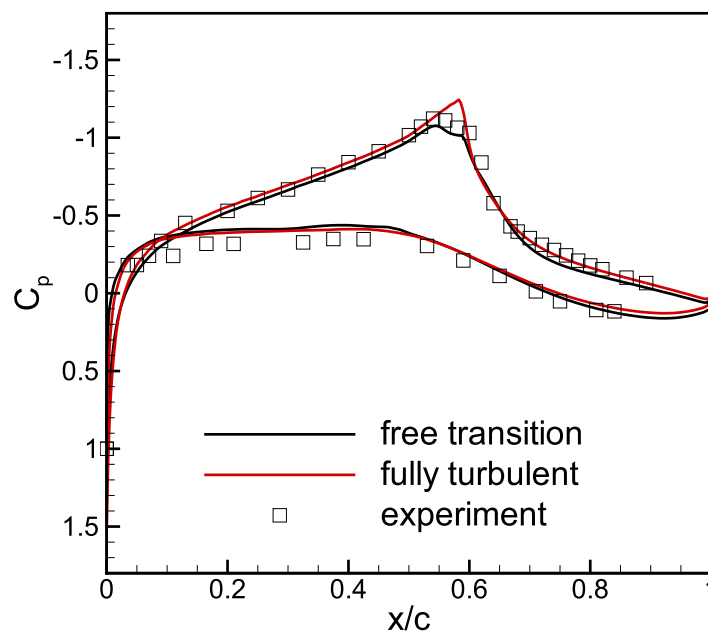

Fig.14 Surface pressure distribution in the central section of B-LFW, M=0.77, α=0°, Re$_c$ =2.6×10^6
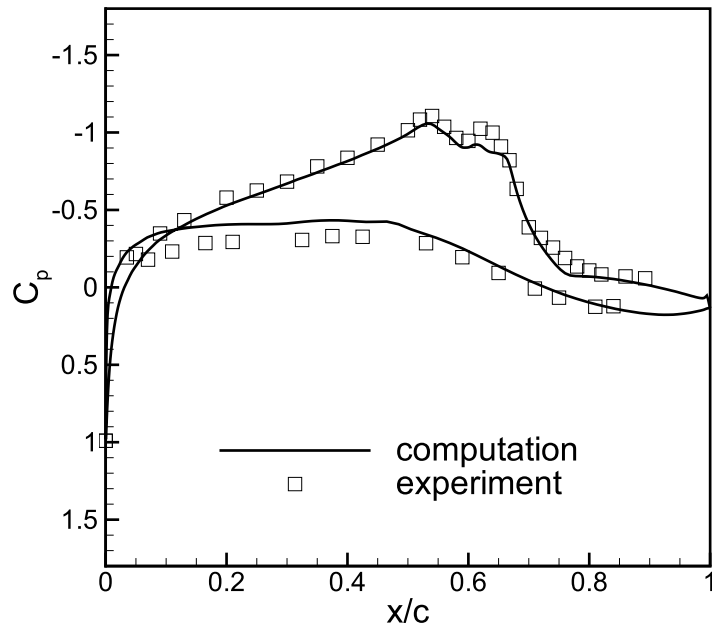
Fig. 15 Surface pressure distribution in the central section of SC-LFW, M=0.77, α=0°, Re$_c$ =2.6×10^6
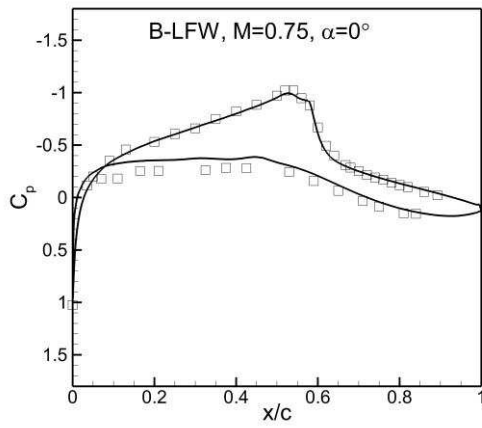
a)
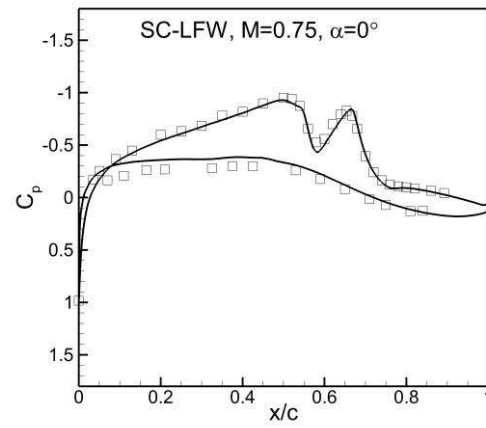
b)
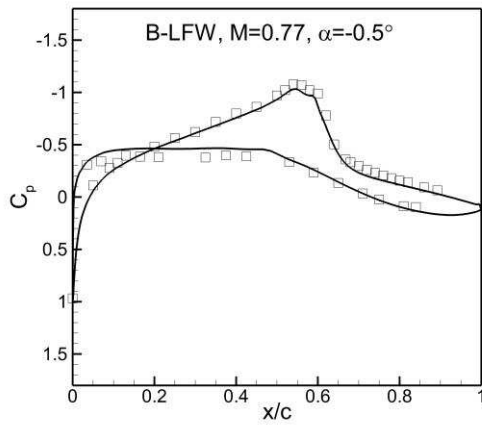
c)
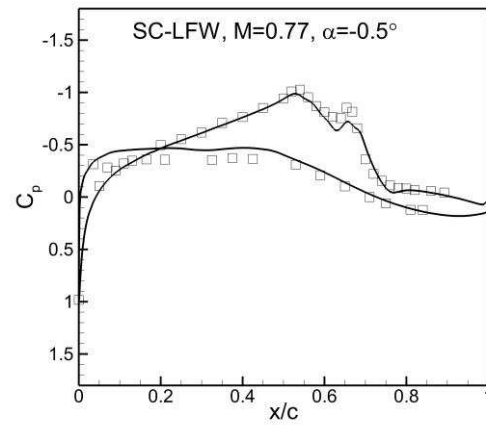
d)
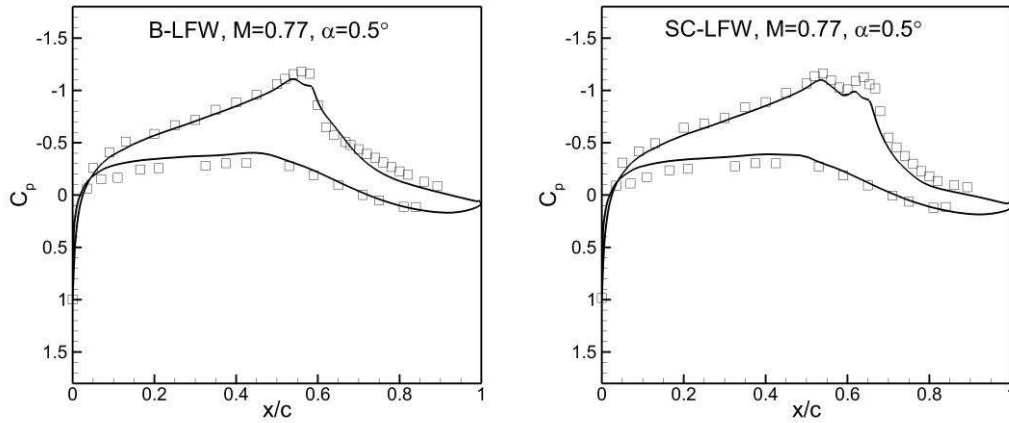
e)   f)

Fig.16 Surface pressure comparison in the central section at some off-design conditions

The surface pressure distributions of B-LFW and SC-LFW at the design condition are compared using computational results in Figure 17. In the central section, the pressure peak decreases with shock control as the shock is weakened with pre-compression. The bumps also shift the shock wave downstream slightly. There is a variation in the surface pressure in the spanwise direction in the bump region which can be attributed to the boundary layer displacement effects of the spanwise flow around the shock control bumps [32]. In the section between two neighboring bumps, surface pressure shows a similar trend to the baseline wing with a further downstream shock wave.
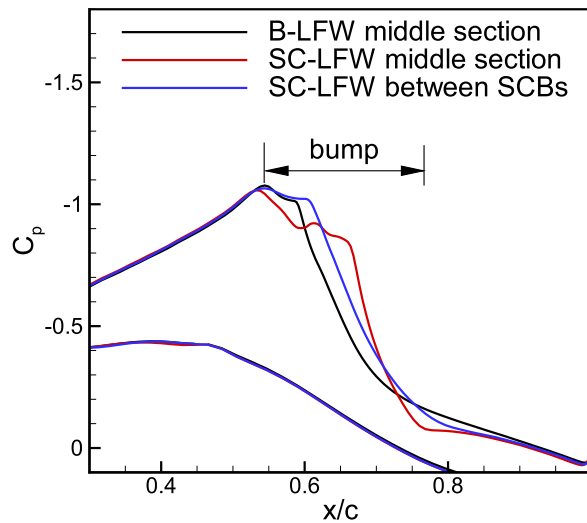

Fig.17 Pressure coefficient comparison, computational results

4.2 Shock control effect on velocity fields

To further examine the effect of the contour bump array on the flow field, Figures 18 and 19 give the velocity magnitude contours of RANS solutions and PIV results at the central section. They show a similar velocity contour which reflects the location and the shape of the shock wave. A normal shock formed on the upper surface of the baseline wing. Velocity contours of B-LFW and SC-LFW obtained by PIV are shown in Figure 19 which show a good correspondence with the RANS solutions. Note that,

due to the limitation of PIV, the measurement could not reach the region near the wing surface.

Both of the experiment and simulation show the original strong shock near x/c=0.6 and the shock strength was significantly reduced and largely spread into gradual compression waves near the surface. Figure 18 also shows that the shock induced boundary layer thickening was also reduced as a result of the weaker shock.
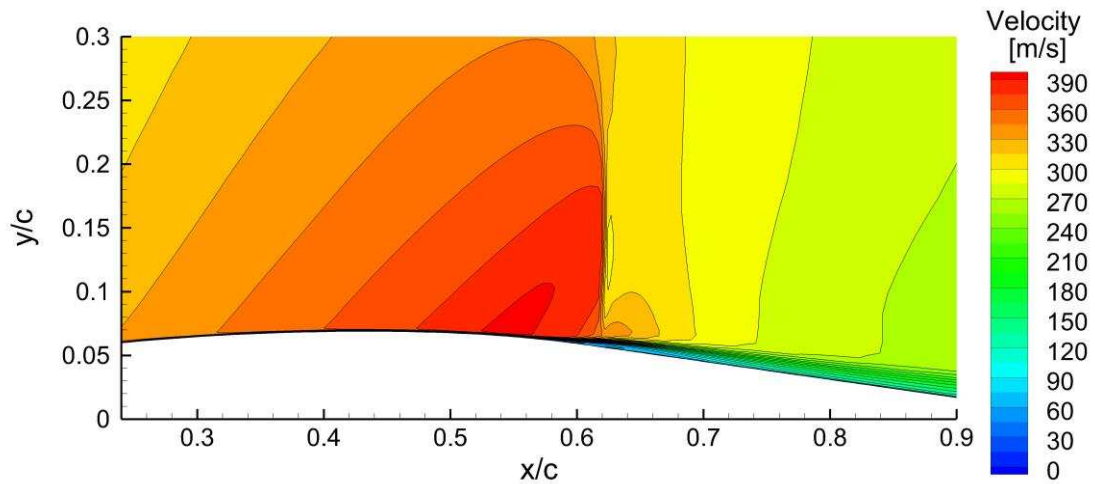
a) Velocity contour of B-LFW
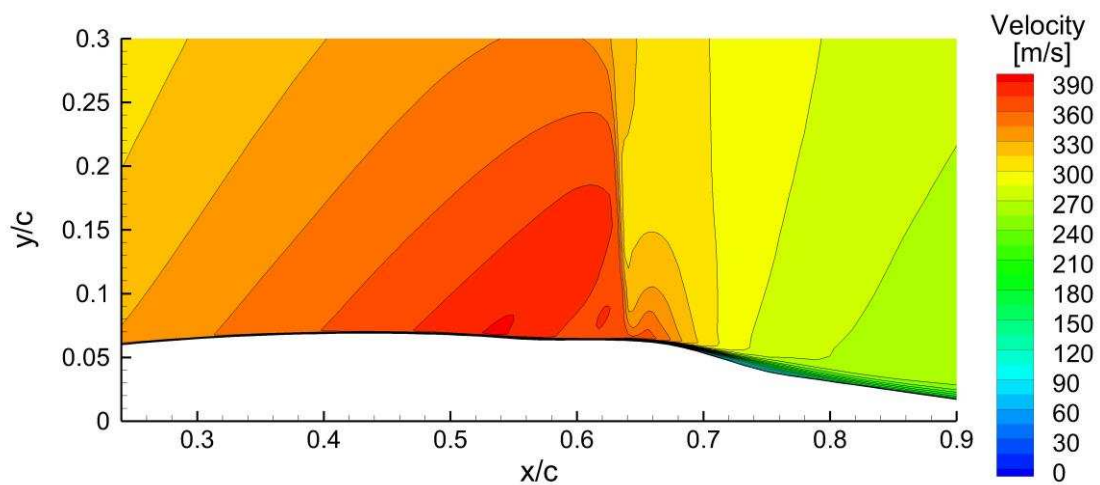
b) Velocity contour of SC-LFW

Fig.18 CFD results of B-LFW and SC-LFW, M=0.77, α=0°, Re_c =2.6×10^6
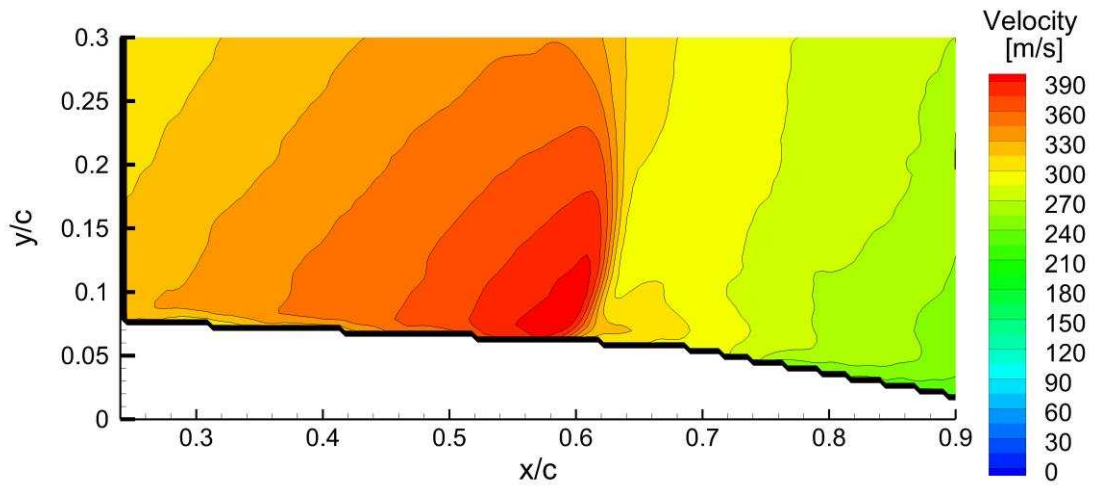
a) Velocity contour of B-LFW
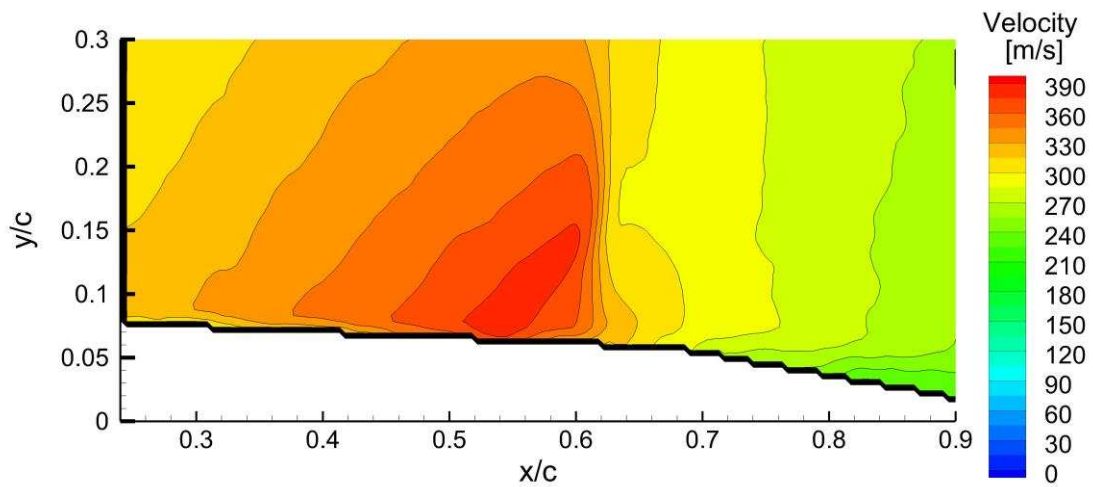
b) Velocity contour of SC-LFW

Fig.19 PIV results of baseline wing (upper) and SCB-wing (lower), M=0.77, α=0°, Re$_c$ =2.6×10^6

4.3 Laminar-Turbulent transition process

Temperature sensitive paint is an optical measurement technique. The paint consists of the temperature-sensitive molecules which could emit fluorescence when excited by a light source and the intensity of fluorescence decreases with increasing temperature. Since the heat transfer rate in turbulent flow is higher than that in laminar flow, there is a temperature difference in laminar and turbulent boundary layers. This difference in temperature is related to the intensity of the emitting fluorescence sensed by the image acquisition system.

Temperature sensitive paint was applied on the suction side of both the baseline and shock-control wing, covering the area between Sections 1 and 2 in the spanwise direction. Figures 20 and 21 show the TSP and computational results of the baseline wing at the design condition. The laminar flow in experiment and computation corresponds to the area with lower values of fluorescence intensity I and intermittency factor γ, respectively while turbulent flow area corresponds to higher values. Figures 20(a) and 21(a) give the intensity and intermittency factor contours between Sections 1 and 2 and the transition onset locations. Figures 20(b) and 21(b) show the fluorescence intensity and intermittency factor distributions extracted from the contours in different spanwise sections away from the central section with pressure taps. The experimental results of these specified spanwise sections

were used to avoid early transition caused by surface roughness. The steep increase of them which could give the location of transition onset, x_{tr}, in experiment (fluorescence intensity) and computation (intermittency factor), respectively, is marked in these figures. Laminar-turbulent transition onset occurred at an approximate chord-wise location of x=0.56c in both experiment and computation from the analysis. It could be seen that the intensity distributions in Figure 20(b) show a more gradual increase while the intermittency factor has an abrupt increase around x=0.56c in Figure 21(b). Therefore, the transition region captured by computation is shorter than that in experiment. In the vicinity of the central section, transition is clearly triggered near the leading edge by the pressure taps placed here in experiment, as seen in Figure 20(a). This transition is attributed to the local surface roughness around the taps.

Figures 22 and 23 give the results of SC-LFW. The transition onset in different sections in experiment varies between x=0.56c and x=0.62c, as seen in Figure 22(a) while in computation, it varies between x=0.59c and x=0.64c. An average value of transition onset location, $x_{tr,avg}$, is labelled in the fluorescence intensity and intermittency factor contours. Therefore, the SCBs could postpone transition onset to a certain degree both in experiment and computation. The transition onset location compares well between experiment and computation although laminar region is a little overestimated in computation in this case.

The intermittency factor contour of SC-LFW shows a small periodical variation in the spanwise direction, as seen in Figure 23(a). In the vicinity of the bump crest region, transition occurred further downstream than that between two neighboring bumps. It is caused by the weaker and further downstream shock wave over bump crest. However, TSP results failed to capture this periodical variation. From the above results, the transition location is collocated around the foot of the shock wave for the laminar flow wings studied here.
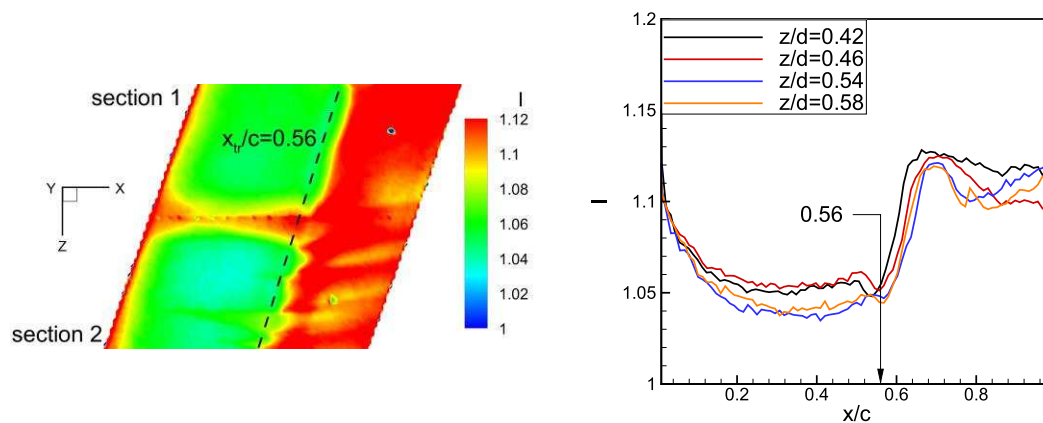

a) Fluorescence intensity contour   b) Fluorescence distributions in different sections

Fig.20 Experimental results of B-LFW at M=0.77, $\alpha=0°$, Re_c =2.6×10^6
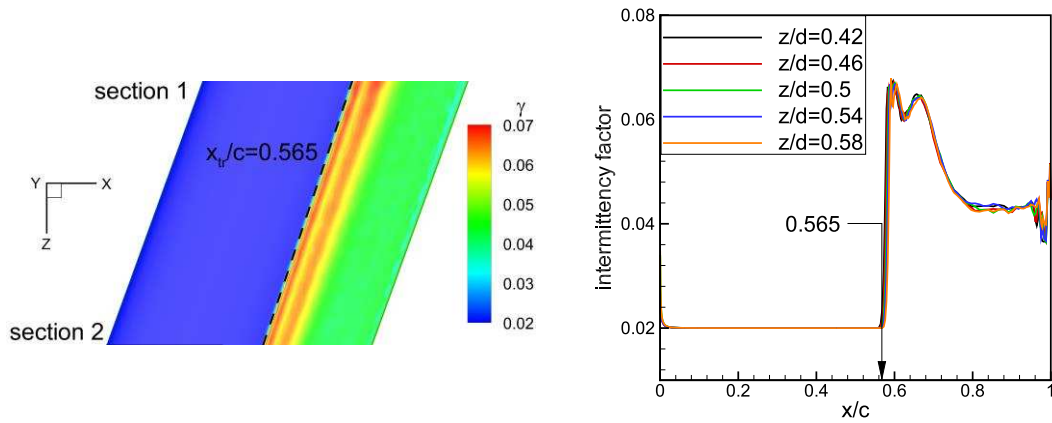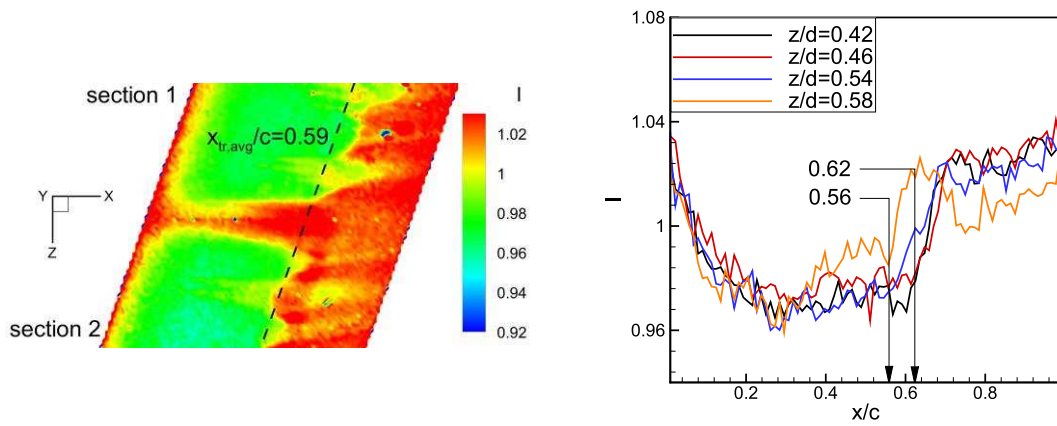
a) Intermittency factor contour

b) Intermittency factor distributions in different sections

Fig.21 Computational results of B-LFW at M=0.77, α=0°, Re_c =2.6×10^6

a) Fluorescence intensity contour

b) Fluorescence distributions in different sections

Fig.22 Experimental results of SC-LFW at M=0.77, α=0°, Re_c =2.6×10^6
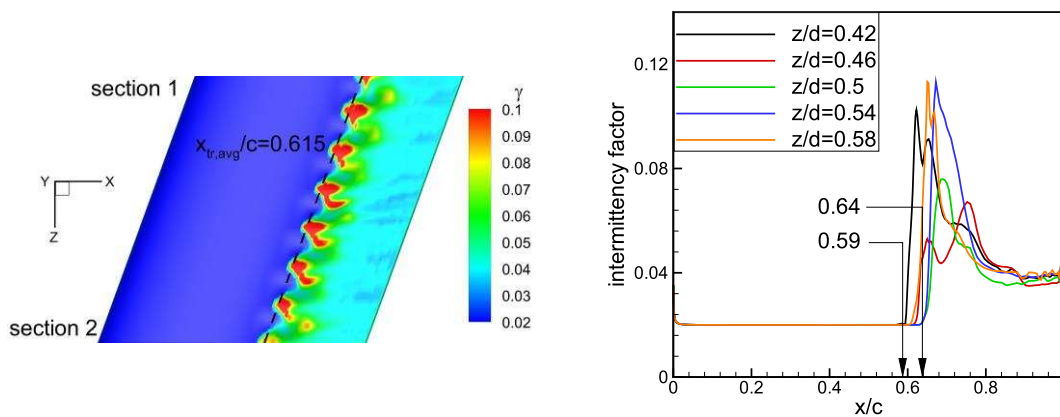
a) Intermittency factor contour

b) Intermittency factor distributions in different sections

Fig.23 Computational results of SC-LFW at M=0.77, α=0°, Re_c =2.6×10^6

In order to look into more details of the transition process, Figure 24 shows the computational results of the intermittency factor contour (top) with streamwise skin friction and pressure distribution (bottom) in the central section of the baseline wing. The negative value of streamwise (x-direction) skin friction $C_{f\,x}$ was used as a suggestion of separated flow. On the lower surface without a shock, transition occurred around 0.45c. On the upper surface, laminar flow developed from the leading edge and a laminar separation bubble induced by shock wave formed at 0.565c in Figure 24(b). Laminar-turbulent transition begins here (0.565c), as seen in the intermittency factor distribution. The fully turbulent flow then reattaches around 0.665c.
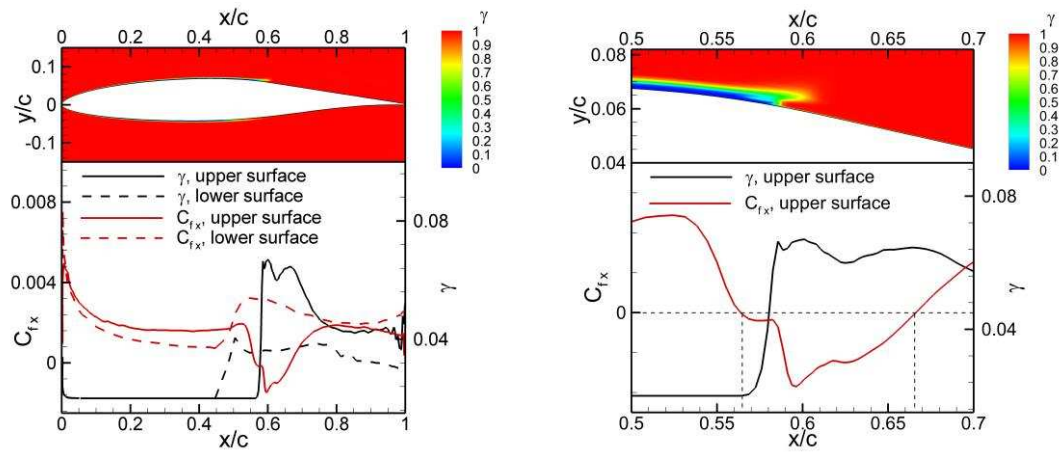
a) Overall trend   b) Magnified on the upper surface

Fig.24 Computed intermittency factor contour (top), streamwise skin friction and intermittency factor distributions (bottom) of B-LFW in the central section

Figure 25 shows the computed intermittency factor contours on the upper surface of B-LFW and SC-LFW in the central section and the section between SCBs (Section 4). In the central section, transition is obviously delayed on the SC-LFW as the shock wave was alleviated by the shock control bumps, as shown in Figure 25(a). However, because of the limited shock control effect in the Section 4, transition location moves little downstream. Figure 26 compares the computed intermittency factor and streamwise skin friction distributions on the upper surface of B-LFW and SC-LFW. In the central section, not only the transition is delayed, but also the separation bubble was almost eliminated, as seen in the skin friction distribution in Figure 26(a). In Section 4, the separation area is reduced a little.
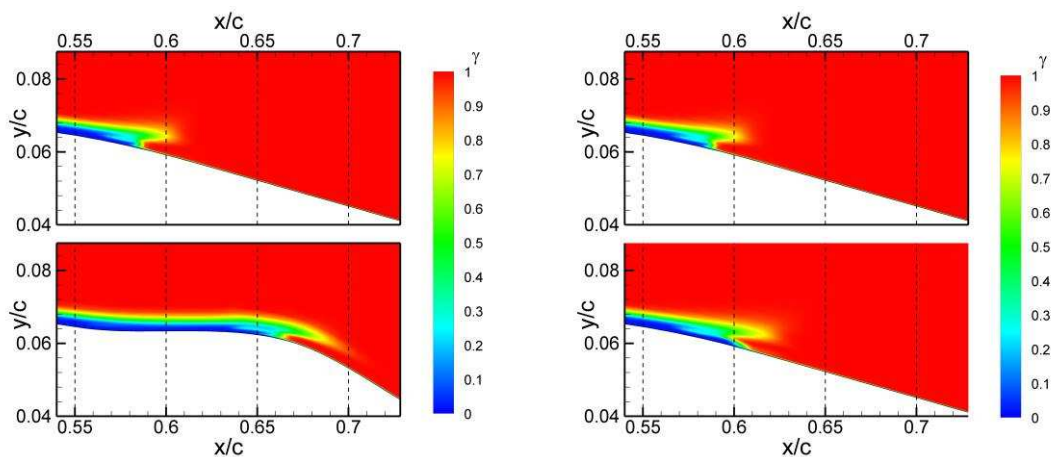
a) Central section   b) Section 4

Fig.25 Computed intermittency factor comparison of B-LFW (top) and SC-LFW (bottom)
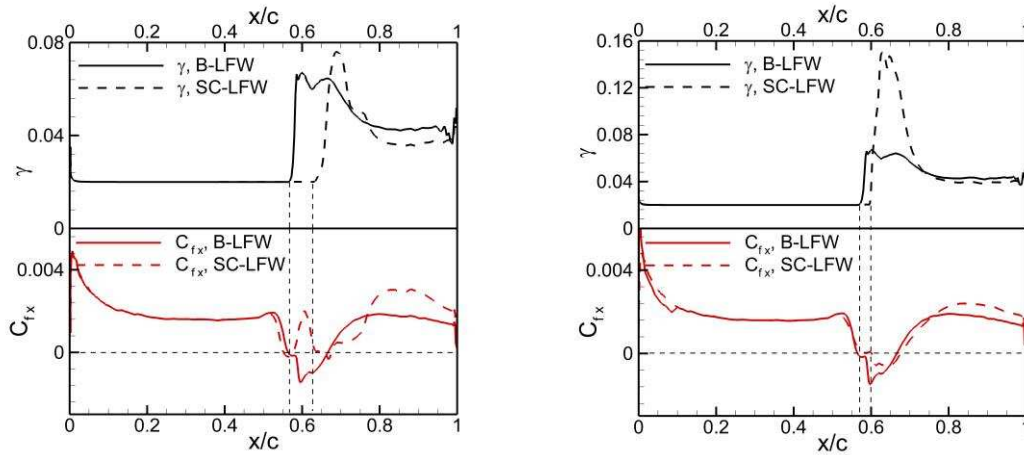
a) Central section   b) Section 4

Fig.26 Computed intermittency factor and streamwise skin friction comparison of B-LFW and SC-LFW

4.4 Shock control effect on lift and drag forces

After the comparison of surface pressure, velocity flow field and the transition location between the experimental data and the computational prediction, some computational results will be given next for the forces on the models. No experimental results for forces are available due to the particular setup for this investigation to integrate the force balance and the potential transonic interference using the wake rakes, which makes the comparison difficult with increased blockage in a relatively small wind tunnel.

The computed force coefficients were obtained by integrating surface pressure and skin friction between the spanwise Sections 3 and 4 for both models. Table 2 gives the lift and drag coefficients at the design condition. The lift increases slightly for the SC-LFW, while the total drag is reduced by 12.25% with 18.5% reduction in pressure drag and 5.0% increase in skin friction drag. The lift-to-drag ratio increases by 24.8% from 18.69 to 23.32. The significant pressure drag reduction comes from the reduced wave drag and the slightly increased skin friction comes from the increased surface area for the wing with the bumps. Robustness of shock control is a crucial factor for design. Figures 27-30 show the shock control effect at some off-design conditions. The shock control bumps at off-design conditions also show some benefits although they are not as effective as those at the design condition. Figures 27 and 29 show effectiveness of the shock control with varying incidence. The benefit of the shock control bumps remains at these off-design conditions. Note for the lower Mach number case in Figures 28 and 30, the shock control shows much less effect due to the weaker shock wave without control.

Table 2 Lift and drag coefficients at M=0.77, α= 0°, Re$_c$ =2.6×10^6

Group	Lift	Drag	Pressure Drag	Skin Friction	L/D

	Coefficient	Coefficient	Coefficient	Drag Coefficient	
B-LFW	0.2484	0.013289	0.009754	0.003535	18.69
SC-LFW	0.2719	0.011661	0.007948	0.003713	23.32
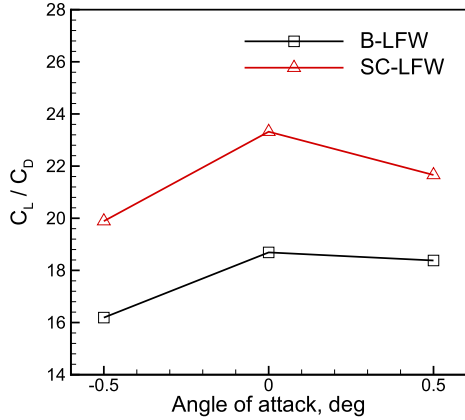
Fig. 27 Lift-to-drag ratio at different angles of attack, M=0.77
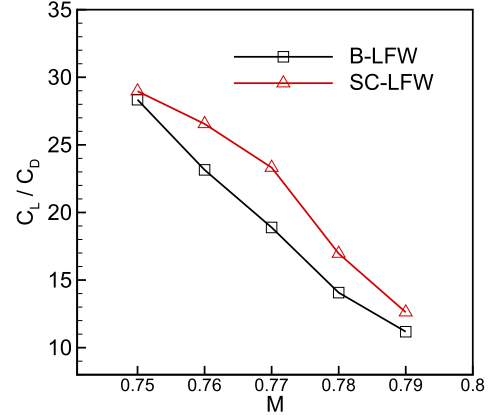

Fig. 28 Lift-to-drag ratio at different Mach numbers, $\alpha=0°$
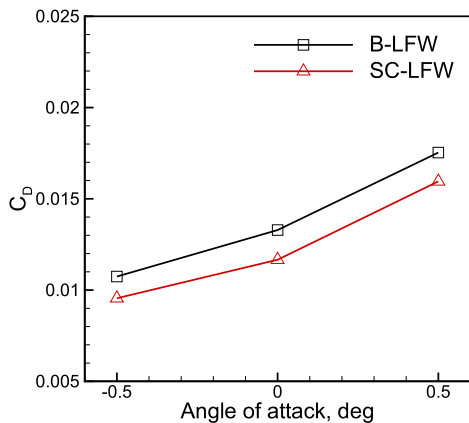
Fig. 29 Drag coefficients at different angles of attack, M=0.77
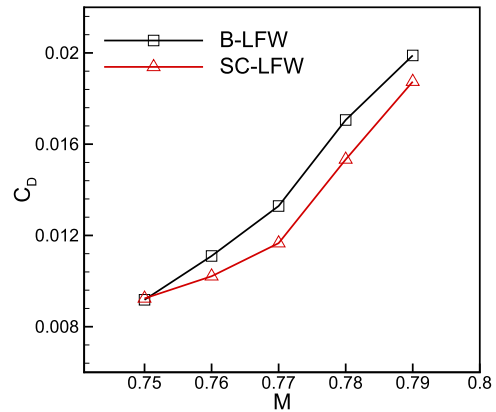
Fig. 30 Drag coefficients at different Mach numbers, $\alpha=0°$

5. Conclusions

The effectiveness of shock control bumps for low sweep transonic natural laminar flow wings has been investigated using a combined experimental and computational approach. An array of 3D contour bumps has been parameterized and implemented on the baseline laminar flow wing. The two key parameters, bump crest and bump height, have been optimized for aerodynamic performance, which was then used for the manufacture of the wind tunnel controlled model. The wind tunnel data and the RANS computational results were presented side-by-side systematically in comparison for surface pressure coefficients, spatial velocity flow field characteristics and transition locations. Some findings are summarized as following:

➢ When the computational model matches the wind tunnel environment with solid walls, the pressure distribution, velocity field, separation pattern, shock wave structure and transition

locations compared well between the experiments and computational simulations.

➤ Three-dimensional shock control bumps have been shown both numerically and experimentally to enable shock control for laminar flow wings at a relative low sweep angle of 20°. The optimized three-dimensional shock control bumps show 18.5% pressure drag reduction with about 5% friction drag penalty at the design point.

➤ The shock control also shows benefits at off-design points for varying incoming flow Mach number and small variation of incidence. The range of the variation is limited by the transonic solid wall constraints.

➤ In the central section, the normal shock converted into a small region of compression waves with a following continuous subsonic expansion of the flow, which was validated in the PIV observation.

➤ Transition on the baseline wing was induced by a laminar separation bubble (with spanwise flow) at the foot of the shock and the shock control bump can slightly delay the transition onset and in the meantime almost eliminated flow separation with small separation bubbles downstream of the shock control bumps.

6. Acknowledgements

7. References

[1]   Kallas, S., Geoghegan-Quinn,M., Darecki,M., Edelstenne, C., Enders, T., Fernandez, E., and Hartman, P., "Flightpath 2050 Europes Vision for Aviation," Tech. Rept., Vol. 98, European Commission, Brussels, Belgium, 2011

[2]   Lammering, T., Anton, E., Risse, K., Franz, K., and Hoernschemeyer, R., "Gains in Fuel Efficiency: Multi-Stop Missions vs. Laminar Aircraft," 11th AIAA Aviation Technology, Integration, and Operations (ATIO) Conference, Virginia Beach, VA, AIAA paper 2011-6885, Sep. 2011.
doi:10.2514/6.2011-6885

[3]   Atkin, C. J., and Courtenay, W.J.A, "Predicting the cruise performance of a retrofit hybrid laminar flow control system," CEAS Aerospace Aerodynamics Research Conference, London, Jun. 2002.

[4]   Abbott, I. H., Von Doenhoff, A. E., and Stivers, L., Jr., "Summary of Airfoil Data," NACA TR-824, 1945.

[5]   Somers, D. M., "Design and Experimental Results for a Natural-Laminar-Flow Airfoil for General Aviation Applications," NASA TP-1865, 1981.

[6]   Holmes, B.J., and Obara, C.J., "Observations and Implications of Natural Laminar Flow on Practical Airplane Surfaces," Journal of Aircraft, Vol. 20, No. 12, 1983, pp. 993-1006.
doi:10.2514/3.48203

[7]   Horstmann, K., Redeker, G., Quast, A., Dressler, U., and Bieler, H., "Flight Tests with a Natural Laminar Flow Glove on a Transport Aircraft," Flight Simulation Technologies Conference and Exhibit, Dayton, Ohio,

AIAA Paper 1990-3044, Sept. 1990.

[8]   Anderson, B. T., and Meyer, R. R., "Effects of Wing Sweep on In-Flight Boundary Layer Transition for a Laminar Flow Wing at Mach Numbers from 0.60 to 0.79," NASA TM-101701, 1990.

[9]   Fauci, R., Nicolì, A., Imperatore, B., and Cella, U., "Wind Tunnel Tests of a Transonic Natural Laminar Flow Wing," 25th AIAA Aerodynamic Measurement Technology and Ground Testing Conference, San Francisco, Califonia, AIAA paper 2006-3638, 2006.

[10] Cella, U., Quagliarella, D., Donelli, R., and Imperatore, B., "Design and Test of the UW-5006 Transonic Natural-Laminar-Flow Wing," Journal of Aircraft, Vol. 47, No. 3, 2010, pp. 783-795.
      doi:10.2514/1.40932

[11] Hue, D., Vermeersch, O., Bailly, D., Brunet, V., and Forte, M., "Experimental and Numerical Methods for Transition and Drag Predictions of Laminar Airfoils," AIAA Journal, Vol. 53, No. 9, Sept. 2015, pp. 2694–2712.
      doi:10.2514/1.J053788

[12] Hue, D., Vermeersch, O., Duchemin, J., Colin, O., Tran, D., "Wind-Tunnel and CFD Investigations Focused on Transition and Performance Predictions of Laminar Wings," AIAA Journal, Vol. 56, No. 1, 2017, pp. 132-145.
      doi:10.2514/1.J056088

[13] Xu, J., Fu, Z., Bai, J., Zhang, Y., Duan, Z. and Zhang, Y., "Study of Boundary Layer Transition on Supercritical Natural Laminar Flow Wing at High Reynolds Number through Wind Tunnel Experiment," Aerospace Science and Technology, Vol. 80, 2018, pp 221-231.
      doi:10.1016/j.ast.2018.07.007

[14] Williams, G., "Aerospace Technology Demonstration: BLADE, the Flagship Laminar Flow Project within the Clean Sky Programme," SAE Technical Paper No. 2017-01-2016, Forth Worth, Texas, Sep. 2017.
      doi:10.4271/2017-01-2016

[15] König, J., and Thomas, H., "The clean sky smart fixed wing aircraft integrated technology demonstrator: Technology targets and project status," Proceedings of International Congress of the Aeronautical Science, Vol. 5, No. 3, France, 2010.

[16] Qin, N., "Drag Reduction for Transonic Wings Combining Reduced Wing Sweep with Shock Control," Invited Keynote Lecture, 28th International Symposium on Shock Waves, Vol. 1, Springer-Verlag, Berlin, Heidelberg, Jan. 2012, pp. 45-53.
      doi:10.1007/978-3-642-25688-2_7

[17] Poll DIA, "Transition in the Infinite Swept Attachment Line Boundary Layer." The Aeronautical Quarterly, Vol. 30, No.4, 1979, pp. 607-629.
      doi:10.1017/S0001925900008763

[18] Campbell, R.L., and Lynde, M.N., "Natural Laminar Flow Design for Wings with Moderate Sweep," 34th AIAA Applied Aerodynamics Conference, Washington D.C., AIAA paper 2016-4326, 2016.
      doi:10.2514/6.2016-4326

[19] Joslin, R.D., "Aircraft Laminar Flow Control," Ann. Rev. Fluid Mech, Vol. 30, No. 1, 1998, pp. 301–329.
      doi:10.1146/annurev.fluid.30.1.1

[20] Schrauf, G., "Stability Analysis of the F100 Flight Experiment—a Second Look," Diamler-Benz Aerospace Airbus, ELFIN II Rept. 173, Bremen, Germany, Jan. 1996.

[21] Reed, H. L., and Saric, W. S., "Transition Mechanisms for Transport Aircraft," 38th Fluid Dynamics Conference and Exhibit, Seattle, Washington, AIAA Paper 2008-3743, June 2008.
      doi: 10.2514/6.2008-3743

[22] Crouch, J.D., "Boundary-Layer Transition Prediction for Laminar Flow Control (Invited)," 45th AIAA Fluid Dynamics Conference, Dallas, Texas, AIAA paper 2015-2472, 2015.

doi:10.2514/6.2015-2472

[23] Fujino, M., "Design and Development of the Honda Jet", Journal of Aircraft, Vol. 42, No. 3, 2005, pp. 755-764.

doi:10.2514/1.12268

[24] Pearcey, H.H., "Shock-Induced Separation and Its Prevention by Design and Boundary Layer Control," Boundary Layer and Flow Control, Vol. 2, Pergamon Press, New York, 1961.

doi:10.1016/C2013-0-08248-5

[25] Ashill, P. R., Fulker, J. L., and Shires, A., "A Novel Technique for Controlling Shock Strength of Laminar-Flow Aerofoil Sections," Proceedings of the 1st European Forum on Laminar Flow Technology, Hamburg, Mar. 1992, pp. 175-183.

[26] Stanewsky, E., Delery, J., Fulker, J., and de Matteis, P., "Synopsis of the Project EUROSHOCK II," Notes on Numerical Fluid Mechanics and Multidisciplinary Design: Drag Reduction by Shock and Boundary Layer Control—Results of the Project EUROSHOCK II, Vol. 80, Springer-Verlag, Berlin, Heidelberg, 2002, pp. 1-124.

[27] Knauer, A., "Performance Improvement of Transonic Airfoils Through Contour Modifications in the Shock Region," DLR, German Aerospace Center Research Rept. 1998-03, 1998; also Ph.D. Thesis, Universität Hannover, Hannover, Germany, 1998.

[28] Birkemeyer, J., "Drag Minimization on a Transonic Wing by Ventilation and Adaptive Contour Bumps," DLR, German Aerospace Center Research Rept. 1999-28, 1999; also Ph.D. Thesis, Universität Hannover, Hannover, Germany, 1999.

[29] König, B., Pätzold, M., Lutz, T., and Krämer, E. "Numerical and Experimental Validation of Three-Dimensional Shock Control Bumps," Journal of Aircraft, Vol. 46, No. 2, 2009, pp. 675–682.

doi:10.2514/1.41441

[30] Birkemeyer, J., Rosemann, H., and Stanewsky, E., "Shock Control on a Swept Wing," Aerospace Science and Technology, Vol. 4, No.3, 2000, pp. 147-156.

doi:10.1016/S1270-9638(00)00128-0

[31] Qin, N., Monet, D., and Shaw, S. T., "3D Bumps for Transonic Wing Shock Control and Drag Reduction," CEAS Aerospace Aerodynamics Research Conference, Cambridge, England, UK, 2002.

[32] Qin, N., Wong, W.S., and Le Moigne, A., "Three-Dimensional Contour Bumps for Transonic Wing Drag Reduction," Proceedings of the Institution of Mechanical Engineers, Part G, Journal of Aerospace Engineering, Vol. 222, No. 5, 2008, pp. 619-629.

doi:10.1243/09544100JAERO333

[33] Deng, F., Qin, N., "Quantitative Comparison of 2D and 3D Shock Control Bumps for Drag Reduction on Transonic Wings," Proceedings of the Institution of Mechanical Engineers, Part G, Journal of Aerospace Engineering, 2018.

doi:10.1177/0954410018778815

[34] McIntosh, S.C., and Qin, N., "The Influence of Transition Onset Location on the Performance of Shock Control Bumps," Aeronautical Journal, Vol. 117, No. 1196, 2013, pp. 1137–1151.

doi:10.1017/S0001924000008678

[35] Colliss, S. P., Babinsky, H., Nübler, K., and Lutz, T., "Vortical Structures on Three-Dimensional Shock Control Bumps," AIAA Journal, Vol. 54, No. 8, 2016, pp. 2338-2350.

doi:10.2514/1.J054669

[36] Ogawa, H., Babinsky, H., Pätzold, M., and Lutz, T., "Shock-Wave/Boundary-Layer Interaction Control Using Three-Dimensional Bumps for Transonic Wings," AIAA journal, Vol. 46, No. 6, 2008, pp. 1442-1452.
doi:10.2514/1.32049

[37] Wong, W. S., Qin, N., Sellars, N., Holden, H. A., and Babinsky, H., "A Combined Experimental and Numerical Study of Flow Structures over Three-Dimensional Shock Control Bumps," Aerospace Science and Technology, Vol. 12, No. 6, 2008, pp. 436–447.
doi:10.1016/j.ast.2007.10.011

[38] Bruce, P. J. K., and Colliss, S. P., "Review of Research into Shock Control Bumps," Shock Waves, Vol. 25, No.5, 2015, pp. 451-471.
doi:10.1007/s00193-014-0533-4

[39] Raffel, M., Willert, C.E., Scarano, F., Kähler, C.J., Wereley, S.T., and Kompenhans, J., Particle Image Velocimetry: a Practical Guide, 2nd ed., Springer International Publishing , 2018.
doi:10.1007/978-3-319-68852-7

[40] Ciarella, A., and Lawson, S., "Use of a Ring Wing Model to Investigate Factors Affecting Transition Measurement Using Temperature Sensitive Paint and Hot Films in Transonic Flow," 55th AIAA Aerospace Sciences Meeting, Grapevine, Texas, AIAA paper 2017-1217, 2017.
doi:10.2514/6.2017-1217

[41] Menter, F.R., Langtry, R.B., Likki, S.R., Suzen, Y.B., Huang, P.G., and Völker, S., "A Correlation-based Transition Model Using Local Variables – Part I: Model Formulation," Journal of Turbomachinery, Vol. 128, No. 3, 2004, pp. 413–422.
doi:10.1115/1.2184352

[42] Menter, F.R., Langtry, R.B., Likki, S.R., Suzen, Y.B., Huang, P.G., and Völker, S., A Correlation-based Transition Model Using Local Variables – Part II: Test Cases and Industrial Applications," Journal of Turbomachinery, Vol. 128, No. 3, 2004, pp. 423–434.
doi:10.1115/1.2184353

[43] Lin, Y., Robinson, T., Early, J., Riordan, D., Tweedie, J. and Magee, L., "Implementation of Menter's Transition Model on an Isolated Natural Laminar Flow Nacelle," AIAA journal, Vol. 49, No.4, 2011, pp. 824-835.
doi:10.2514/1.J050890

[44] Wilcox, D.C., Turbulence Modeling for CFD, AIAA, DCW Industries, Inc, La Canada, California, 2006.